China Instrument and Control Society
Instrumentation
INSTRUMENTATION, Vol. 13, No. 2, June 2026
https://doi.org/10.15878/j.instr.202600376

Article-Intelligent Detection & Fault Diagnosis

Aero-engine Air Path Fault Diagnosis via FGO-1DCNN-LSTM

Luyao He[1], Mingzheng Liu[1*], Ximeng Wang[1*], Bo Hu[2], Bin Liu[1], Siying Guo[1]

[1] College of lnformation Science and Engineering,Shenyang University of Technology, Shenyang, Liaoning, China

[2] Key Laboratory of Nondestructive Testing (Ministry of Education), Nanchang Hangkong University, Nanchang, Jiangxi, China

[*] Corresponding author email: 1585728122@qq.com , 3260972617@qq.com

Abstract: To address the shortcomings of existing fault diagnosis models for aero-engine gas path components, such as weak feature extraction capabilities and low diagnostic accuracy, this study proposes a fault diagnosis model underpinned by the Fungal Growth Optimization (FGO) algorithm (FGO-1DCNN-LSTM). This model integrates a 1D convolutional neural network (1DCNN) and a long short-term memory network (LSTM). LSTM's strength in extracting temporal features compensates for the limitations of 1DCNN in processing time-series data. A split-path convolutional fusion module is introduced into the 1DCNN, enabling parallel input of sensor data, thus enhancing both the network's extraction capabilities and efficiency. Simultaneously, the FGO algorithm is incorporated to tackle the issue of hyperparameter optimization. To validate the model's performance, training and validation experiments were conducted using the N-CMAPSS dataset, which covers fault data under three typical operating conditions: low-altitude low-velocity, higher-altitude and higher-velocity, and high-altitude high-velocity. Experimental results indicate that the FGO-1DCNN-LSTM model attains fault diagnosis accuracies of 90.74%, 91.67%, and 94.44% under three operating condition. In comparison with the unoptimized 1DCNN-LSTM model, its diagnostic accuracy is improved by 2.78%, 10.19%, and 3.7%, respectively. The results provide evidence that the FGO-1DCNN-LSTM model can effectively achieve accurate identification and diagnosis of faults in aero-engine gas path components.

Keywords: air pathway; fungal growth optimization algorithm (FGO); 1DCNN; LSTM; data-driven approach

Citation: Luyao He, Mingzheng Liu, Ximeng Wang, Bo Hu, Bin Liu, Siying Guo."Aero-engine Air Path Fault Diagnosis via FGO-1DCNN-LSTM." Instrumentation 13, no.2 (June 2026). https://doi.org/10.15878/j.instr.202600376

1 Introduction

Aero engines typically need to operate stably and continuously under extremely harsh operating conditions, which places stringent requirements on the safety and reliability of the equipment[1]. Once an aircraft engine experiences gradual performance degradation or sudden mechanical failure, it can trigger a chain of failures such as a sudden drop in thrust or excessive vibration, leading to catastrophic flight accidents[2,3]. Related studies have shown that more than half of the failure cases of aero engines are caused by abnormal operating conditions of the air path components[4]. The air path components of aero engines mainly include the fan, compressor, combustion chamber, turbine and tail nozzle, which constitute the key path for power generation and energy transfer[5]. Because the gas circuit components are subjected to extreme working conditions for a long time, they are prone to failure and the failure modes are complex and diverse[6]. It follows that the timely diagnosis and identification of gas path malfunctions in aero engines are essential.

Research on fault diagnosis of aero-engine air circuit components began in the 1960 s[7], Currently, the main diagnostic methods for aero-engine gas path components fall into three categories: methods for establishing diagnostic models based on mechanisms, and diagnostic

methods based on expert prior knowledge and diagnostic methods leveraging data-driven frameworks[8]. Analytical model-based diagnostic methods simulate engine operating conditions by establishing mathematical frameworks such as aerodynamic thermodynamic equations and component-level models, and locate faults by combining the deviation between sensor data and model output[9]. In recent years, algorithms such as Kalman filtering and weighted least squares have been continuously iterated in the optimization based on analytical models[10]. Guido Herrmann et al. proposed an effective emission control strategy for aero-engines, aiming to solve the challenges brought about by the uncertainty of the state and parameters of analytical models[11]. Jia Zihao et al. formulated a multi-state gas-path analysis approach and a fault principal factor screening strategy to address the problem of analytical model identification. Nonlinear feature extraction was achieved through least squares fitting, which reduced the diagnostic error in the verification of turbofan engines[12]. However, the accuracy of analytical model-based diagnostic methods relies heavily on the engine's internal parameters, and the modeling complexity of its dynamic coupling effect limits the real-time diagnostic capability and results in low diagnostic efficiency[13].

Empirical knowledge-based diagnostic methods are represented by expert systems, fuzzy logic and hierarchical analysis, which rely on domain knowledge bases and rule reasoning to achieve fault diagnosis[14]. However, such methods face problems such as lagging knowledge base updates and insufficient rule interpretability. Especially when dealing with failure modes of new material components, the reliability of diagnosis decreases significantly due to the lack of prior knowledge. Compared with the two methods mentioned above, data-driven fault diagnosis methods have significant advantages. They can avoid the complex modeling and solution process based on mechanisms, overcome the problem of insufficient prior knowledge, and have numerous advantages such as high sensitivity, enhanced robustness and superior generalizability in fault diagnosis tasks. Typical data-driven fault diagnosis methods comprise neural networks, decision trees, and support vector regression[15-17].

Deep learning, as a data-driven method for deeper networks, is suitable for processing massive quantities of information data and can extract deeper features from the data to achieve accurate fault diagnosis tasks[18-20]. In deep learning methods, Convolutional Neural Network (CNN), due to their unique convolutional concept, can deeply mine the spatial features of data, thereby enabling their widespread application in fault diagnosis. However, due to the limitations of their network structure, they are not sensitive to the temporal dimension features of data. Long Short-Term Memory (LSTM) architectures constitute a refined variant of recurrent neural networks, making them highly appropriate for deriving features from extended sequence data. They can store longer memories and excel at incorporating long-term dependencies into their structure, providing excellent results and performance when dealing with long-term data sequences. Therefore, this study adopts a method combining CNN and LSTM networks to establish a fault diagnosis model for aero-engine air circuits, achieving the goal of diagnosing aero-engine air circuit faults. First, a one-dimensional convolutional neural network (1DCNN) is used to extract the spatial features of aero-engine air circuit fault data. Second, LSTM is used to extract the temporal features of aero-engine air circuit fault data. By fusing the 1DCNN and LSTM neural network models and introducing a multi-feature fusion module into the 1DCNN, the features of the fault data can be captured more accurately, completing the construction of the 1DCNN-LSTM model. Finally, the Fungal Growth Optimization (FGO) algorithm[21] was introduced to predict the hyperparameters that need to be manually adjusted in the model, thus enhancing both the model's accuracy and computational efficiency. Figure 1 presents the research procedure of this study.

2 1DCNN-LSTM-based Fault Diagnosis Model for Aero-engine Air Paths

2.1 1DCNN

CNN is a neural network that uses special linear discrete convolution operations, and it has high fault tolerance and robustness in feature learning[22]. Since the sensors of the aero-engine air path components are one-dimensional time-series data[23], but the convolution kernels of traditional CNN networks are two-dimensional, it is necessary to construct one-dimensional convolution kernels to realize the basic structure of 1DCNN network, so as to better apply to aero-engine air path fault data. In addition, By introducing branch convolution and multi-feature fusion modules, the method processes data from different sensors through parallel branch convolutions followed by fusion, enabling parallel data input and thereby enhancing the model's efficiency and capability in feature extraction. The formula of the feature fusion module is described as follows:

$$F_{fusion} = \sum_{i=1}^{n} \alpha_i \cdot F_i \tag{1}$$

In the equation, represents the weight of the i-th feature (satisfying $\sum_{i=1}^{n} \alpha_i = 1$), which is adaptively learned through network training. Specifically, these weights are learnable parameters of the model. During training, the network continuously adjusts the value of $\alpha_i$according to the loss function, enabling the final fused features to more effectively diagnose faults. The structure of the 1DCNN used in this study is illustrated in Figure 2.

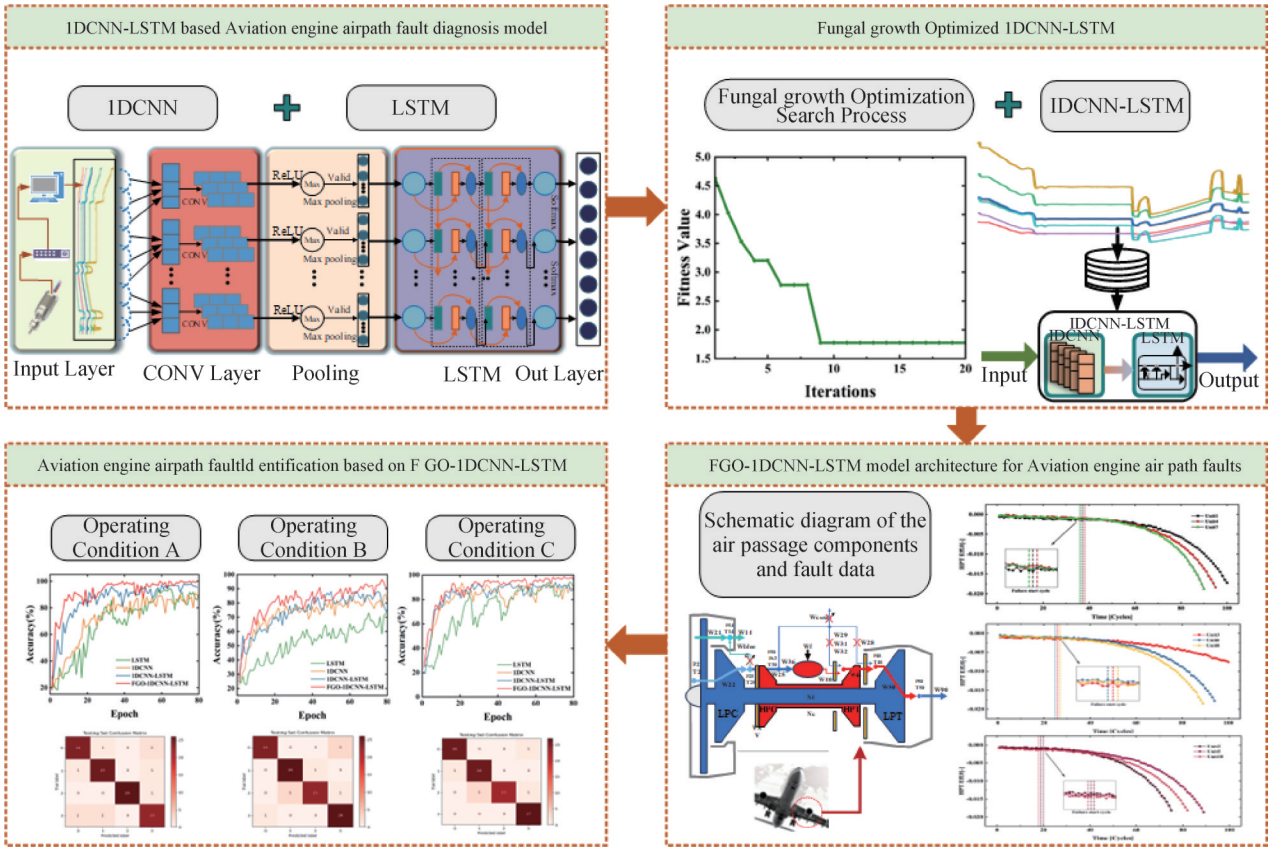

Fig.1 Architectural Framework Diagram

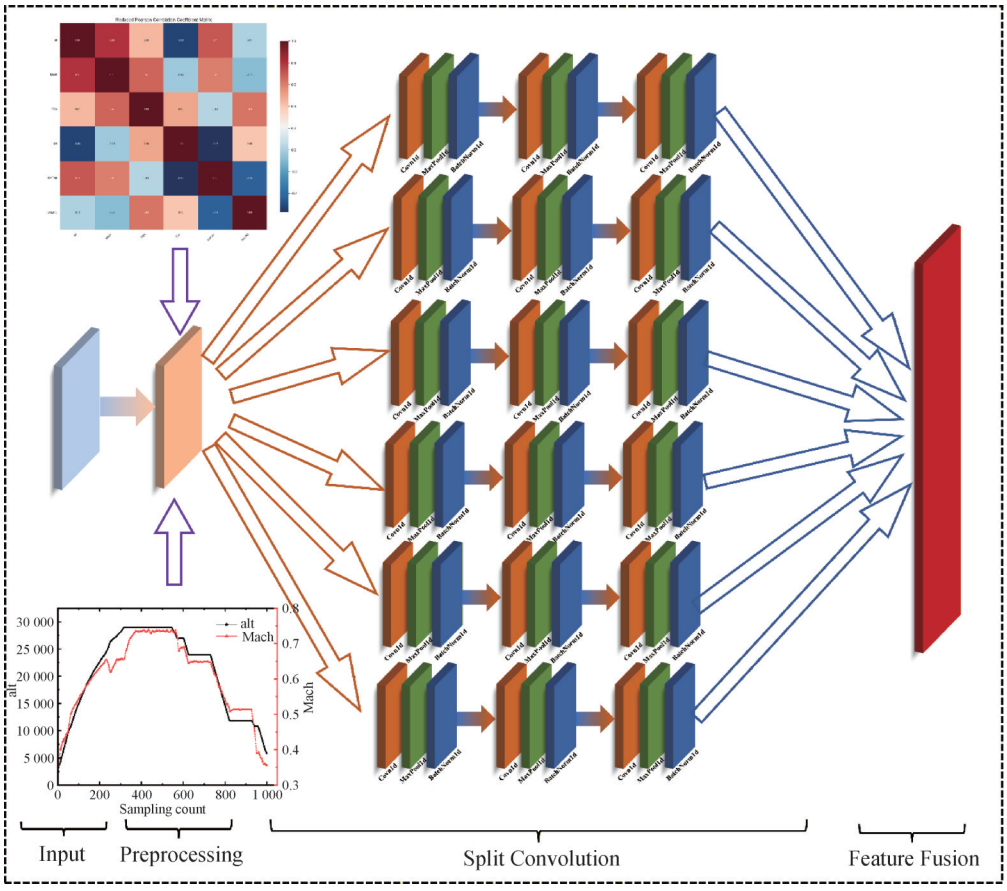

Fig.2 1DCNN network structure

2.2 1DCNN-LSTM Fault Diagnosis Model

LSTM uses "cell state" as the core information flow[24,25], and its structure is shown in Figure 3. In this study, a two-layer LSTM is constructed to improve the model's ability to model long sequence dependencies through two layers of temporal feature extraction.

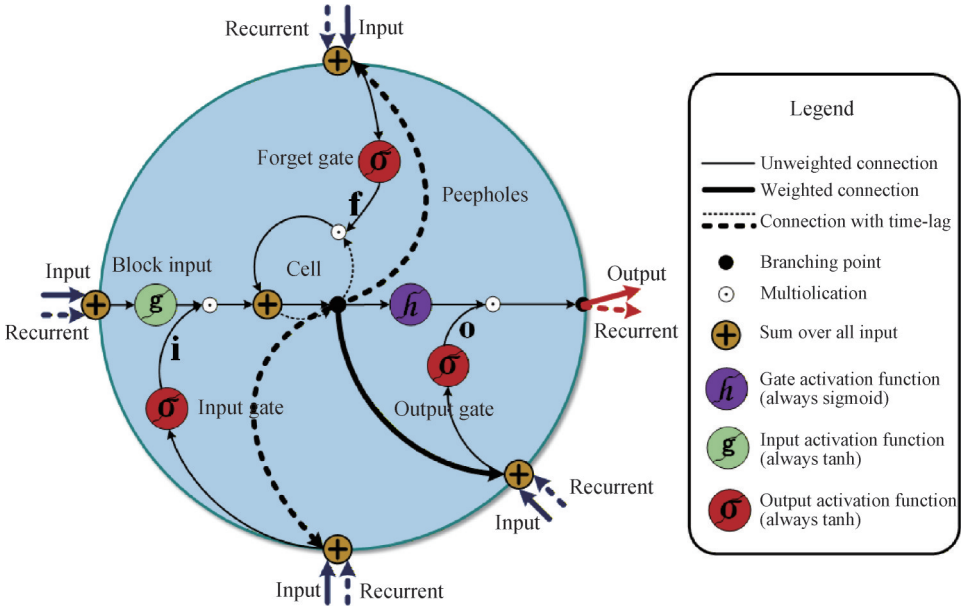

Fig.3 LSTM network structure

Given the significant differences between 1DCNN and LSTM in feature extraction mechanisms, this study proposes to integrate the two models in series, leveraging the powerful extraction capabilities of LSTM for time-dimensional features to compensate for the limitations of 1DCNN in this regard, and constructing a 1DCNN-LSTM model to diagnose air path faults in aero-engines. The 1DCNN-LSTM model is illustrated in Figure 4.

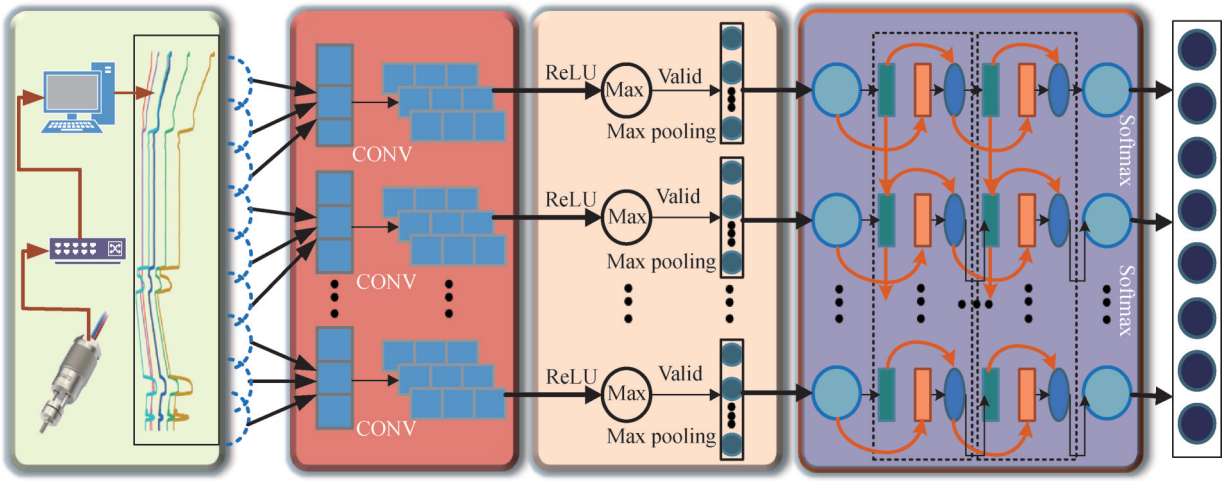

Fig.4 1DCNN-LSTM network structure

2.3 FGO-1DCNN-LSTM Model

To address the hyperparameter tuning problem of 1DCNN-LSTM models, this study introduces the Fungal Growth Optimizer (FGO) algorithm to construct the FGO-1DCNN-LSTM model. FGO is a metaheuristic optimization algorithm based on fungal growth behavior, inspired by three key biological processes in fungi: hyphal tip growth, branching, and spore germination[26]. By simulating the mechanism by which fungi seek nutrients in complex environments, this algorithm balances exploration and exploitation capabilities, effectively solving high-dimensional, multimodal optimization problems.

The framework of the FGO-1DCNN-LSTM aero-engine gas path fault diagnosis model is depicted in Figure 5. First, the sensor data across various working conditions in the N-CMAPSS dataset are analyzed, and the obtained data are downsampled and smoothed to

generate a sample set. The sample set is partitioned into a training set and a test set at an 8: 2 ratio. A 1DCNN-LSTM model is established and the initial interval of hyperparameters is set. The hyperparameters are optimized by the FGO algorithm to achieve the maximum accuracy of the model. The test set is fed into the model, and the Softmax layer's diagnostic results are produced to evaluate the model's performance[27].

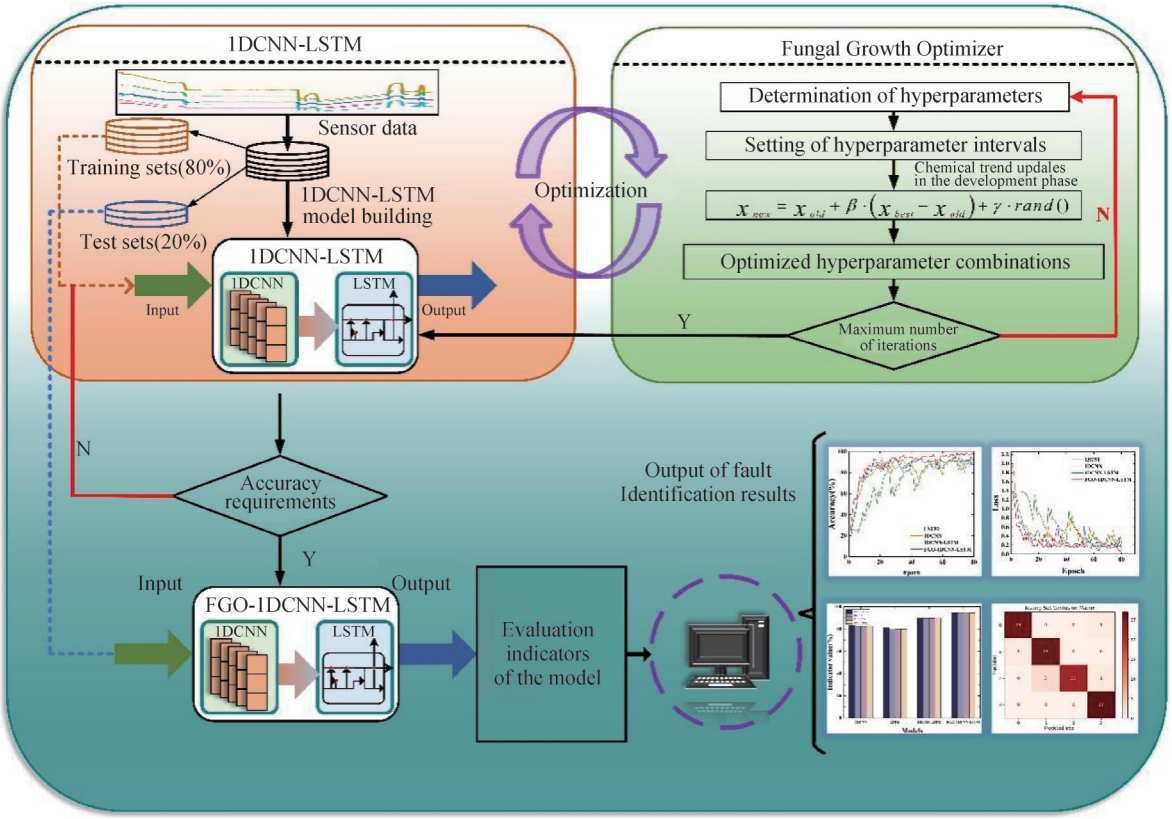

Fig.5 Framework diagram of FGO-1DCNN-LSTM

2.4 Parameters of the FGO-1DCNN-LSTM model

Table 1 illustrates the structural parameters of the 1DCNN-LSTM. After preprocessing, the data is input in parallel into the split convolutional module of the 1DCNN to extract spatial features. The split convolutional module effectively reduces feature aliasing between different sensors. Subsequently, the high-dimensional feature sequence is reduced by pooling and then input into a two-layer LSTM network model after passing through the feature fusion module to further extract temporal features. Finally, the Softmax layer outputs the probability of the result based on the extracted feature information.

Table 1 1DCNN-LSTM architecture parameters

Structural layer	Parameter settings	Enter shape	Output shape
Convolutional layerC1	Conv1d(1, 32)	1,1000	32,500
Convolutional layerC2	Conv1d(32, 64)	32,500	64,250
Convolutional layerC3	Conv1d(64, 128)	64,250	128,125
Feature fusion layer	CrossSensor(6x1)	128,125	256,125
Double layer LSTM	LSTM*2	125,256	125,192
Fully connected layer	Fully connected	125,192	192,256
SoftMax Output layer	Activation:Softmax	192,256	4,1

The initial learning rate, regularization coefficient, and number of hidden layers are chosen as the hyperparameters to be optimized, and are given in Table 2. The quality of the optimization algorithm can be judged by the convergence process of the fitness function, which is defined as follows:

$$\text{Fitness}(\theta) = 1 - \max_{1 \le e \le E} \text{Acc}^{e}_{\text{test}}(\theta) \tag{2}$$

Table 2 Interval setting of the 1DCNN-LSTM hyperparameters

Parameter	Upper and lower limits
Initial learning rate	$[10^{-3},10^{-1}]$
L2 regularization coefficient	$[10^{-3},10^{-2}]$
Number of hidden layer neurons	[64,256]

In the formula, θ is the hyperparameter vector, E is the number of training rounds in the search phase, and $Acc^{e}_{test}(\theta)$ represents the test accuracy in thee-th round.

To verify the reliability of the FGO optimization algorithm, three other algorithms—Bayesian optimization (BO), particle swarm optimization (PSO), and genetic optimization (GA) —were selected for comparison. As shown in Figure 6, The BO, PSO, and GA optimization algorithms were compared respectively, where the fitness function represented the error in accuracy of the test set during the parameter tuning process. After 15 iterations, the convergence of the fitness function of the FGO optimization algorithm substantially outperformed that of the other three optimization algorithms, indicating that the FGO optimization algorithm performs well in finding the objective function of the network introduced in this study.

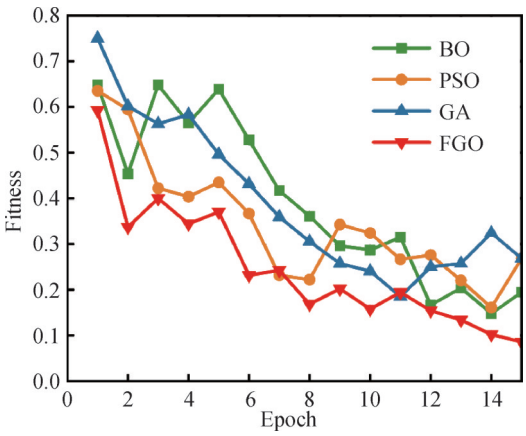

Fig.6 Fitness function graph

3 Data Preprocessing

3.1 Dataset Introduction

The dataset utilized in this study is the publicly available simulation data of aircraft engine performance degradation from NASA's Ames Research Center, namely the N-CMAPSS dataset[28]. The research group led by Manuel used the commercial modular simulation platform CMAPSS to conduct in-depth research on the performance degradation of aircraft engines based on real flight conditions recorded on commercial aircraft. They successfully developed a fresh dataset, named N-CMAPSS, which aims to provide a reference for performance evaluation in the aviation field. CMAPSS simulates real commercial turbofan engines, covering flight altitudes of 0–40 kft, Mach numbers of 0–0.9, sea surface temperatures of -60–103 °F, and thrust of 90 klb.

Manuel et al. used the CMAPSS platform to first randomly set an initial Remaining Useful Life (RUL) for the aero-engine model, and then introduced various types of faults at a certain moment to cause different abnormal performance degradation processes in the aero-engine. Finally, the RUL of the gas path components was continuously calculated. When the RUL was 0, the system was judged to have failed, and the simulation ended. It should be noted that in the N-CMAPSS dataset, each engine has undergone dozens or even hundreds of flight cycles, and each flight cycle simulates one flight mission of the aircraft. Before abnormal degradation, the data is considered healthy. Only when abnormal degradation occurs at a certain moment, the data of all flight cycles from that moment until the engine stops are considered fault data. As shown in Figure 7(a), the x-axis represents the number of cycles, and the y-axis represents the Remaining Useful Life (RUL). The blue part represents the normal degradation process, which is considered healthy data. The red part represents the abnormal degradation process, which is considered fault data. The high-pressure compressor efficiency failure degradation process is shown in Figure 7(b). Through the above steps, we can obtain different fault data[28].

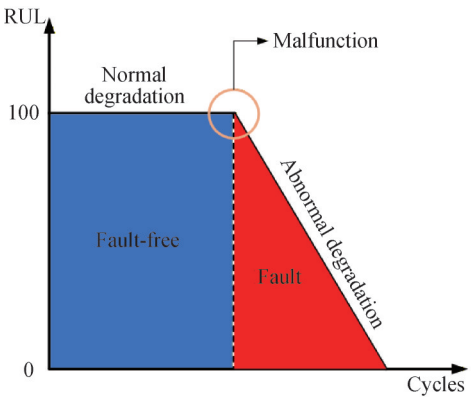

(a) Schematic diagram of the degradation process

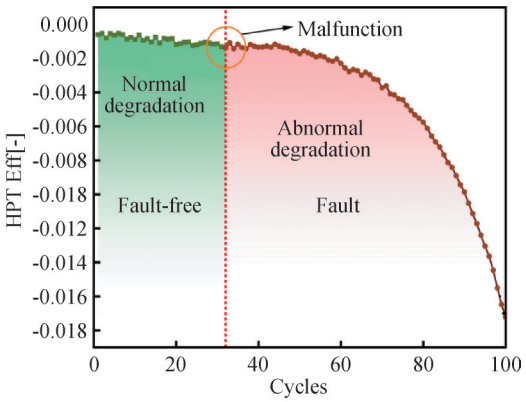

(b) HPT-E Fault Degradation Process

Fig.7 Remaining life degradation model

The N-CMAPSS dataset contains operational data for one flight cycle recorded by sensors. Each flight cycle includes multiple timestamp records, various sensor readings such as pressure, temperature, and fuel flow, and also includes marker information related to engine faults. This dataset provides test results from 128 unique units and covers seven fault categories, each of which affects the flow rate (F) and efficiency (E) of the turbofan engine, involving all the rotating components. Considering the completeness of the data sample and the diversity of faults, this study mainly focuses on the research and analysis of four types of faults: DS01, DS05, DS06 and DS07. The fault labels are shown in Table 3.

Table 3 Types of Faults and Labels

Data	LPC		HPC		LPT		Label
	E	F	E	F	E	F	
DS01	-	-	√	-	-	-	0
DS05	-	-	√	√	-	-	1
DS06	√	√	√	√	-	-	2
DS07	-	-	-	-	√	√	3

Taking DS01 as an example, Figure 8 shows its flight envelope based on its flight altitude and Mach number. The figure shows three colored flight envelopes, corresponding to three flight conditions. Specifically, green represents the flight envelope at low altitude and low speed for a short duration, with an altitude not exceeding 20,000 feet, a speed not exceeding Mach 0.6, and a flight duration typically between 1 and 3 hours. For ease of explanation, we will denote this condition as Condition A. Orange represents the -flight envelope at higher altitude and higher speed for a longer duration, with an altitude not exceeding 30,000 feet, a speed not exceeding Mach 0.7, and a flight duration typically between 3 and 5 hours. Similarly, we will denote this condition as Condition B. Blue represents the flight envelope at high altitude and high speed for an extremely long duration, with an altitude exceeding 30,000 feet, a speed not less than Mach 0.6, and a flight duration typically reaching 5 to 7 hours. We will denote this condition as Condition C, as shown in Table 4.

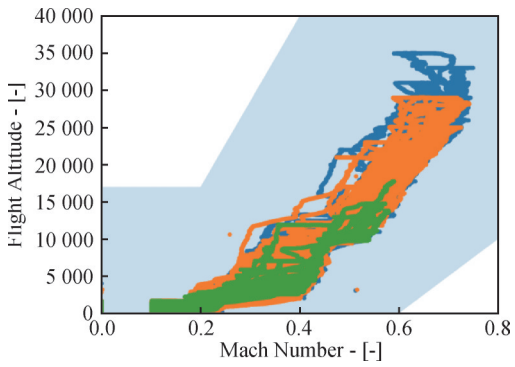

Fig. 8 Flight envelope diagrams under different operating conditions

Table 4 Table of Different Operating Conditions

Condition	Alt(ft)	Speed(Mach)	Time(h)
Operating Condition A	<20000	<=0.6	1–3
Operating Condition B	<30000	<=0.7	3–5
Operating Condition C	>30000	>=0.6	5-7

Figure 9 shows the decrease in high-pressure turbine flow rate with increasing flight cycle count under three operating conditions. Figure 9(a) shows the change in high-pressure turbine efficiency of the three engines with increasing flight cycle count under operating condition A; Figure 9(b) shows the change in high-pressure turbine efficiency of the three engines with increasing flight cycle count under operating condition B; and Figure 9(c) shows the change in high-pressure turbine efficiency of the three engines with increasing flight cycle count under operating condition C. In summary, it can be observed that the failure in operating condition A occurs in the latest cycle, close to 40 cycles; the failure in operating condition B occurs in the middle cycle, around 24 cycles; and the failure in operating condition C occurs in the

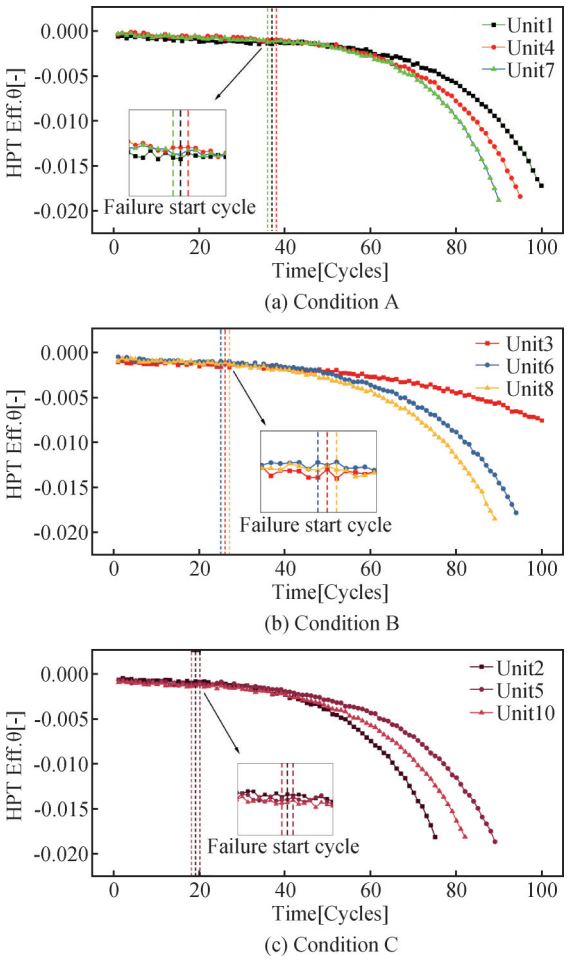

Fig.9 Efficiency variation diagrams of high-pressure turbines under three operating conditions

earliest cycle, less than 20 cycles. This study tested the accuracy of the model under these three operating conditions.

The fault data for each operating condition is composed of flight data recorded by sensors throughout each flight cycle, serving as a sample. For each of the four different faults, 90 flight cycles of data are taken, composed of data from different engines, for a total of 360 data samples. Tables 5, 6, and 7 present the sample composition of condition A, condition B and condition C respectively.

Table 5 Overview of Samples for Operating Condition A

Data	Unit	Cycle	Quantity	Training set	Test set	Label
DS01	1	71-100	90	63	27	0
	4	66-95				
	7	61-90				
DS05	4	70-99	90	63	27	1
	5	38-67				
	8	51-100				
DS06	4	58-87	90	63	27	2
	5	70-99				
	8	62-91				
DS07	4	50-79	90	63	27	3
	5	56-85				
	8	54-83				

Table 6 Overview of Samples for Operating Condition B

Data	Unit	Cycle	Quantity	Training set	Test set	Label
DS01	3	71-100	90	63	27	0
	6	65-94				
	8	60-89				
DS05	1	51-80	90	63	27	1
	3	36-65				
	7	56-85				
DS06	1	49-78	90	63	27	2
	3	36-65				
	7	51-80				
DS07	1	38-67	90	63	27	3
	3	49-78				
	7	49-78				

3.2 Data Preprocessing

Turbofan engines are core equipment in modern aerospace engineering. Thanks to their complex structural design and extremely high manufacturing precision, their performance and efficiency have reached industry-leading levels. The core components of this engine include a fan, low-pressure compressor (LPC), high-pressure compressor (HPC), combustion chamber (CC), low-pressure turbine (LPT), and high-pressure turbine (HPT), as illustrated in Figure 10. These components work together to convert atmospheric air into a high-velocity jet stream, generating powerful thrust to provide the core power for aircraft flight. During operation, air first enters the fan, which increases the total intake air volume and optimizes subsequent combustion efficiency, laying the foundation for air compression and combustion. The air then enters the compressor, where rotating blades compress the air, significantly increasing its density and pressure, delivering a high-pressure, high-temperature working medium to the combustion chamber. Inside the combustion chamber, the compressed air mixes thoroughly with fuel and burns, generating high-temperature, high-pressure combustion gas. Finally, this combustion gas flows through the turbine and is ejected at high speed. The turbine absorbs energy from the combustion gas and converts it into rotational kinetic energy, driving the compressor to continuously compress more air, thus forming a stable cyclical working process.

Table 7 Overview of Samples for Operating Condition C

Data	Unit	Cycle	Quantity	Training set	Test set	Label
DS01	2	46-75	90	63	27	0
	5	60-89				
	10	53-82				
DS05	2	51-80	90	63	27	1
	6	38-67				
	9	40-69				
DS06	2	49-78	90	63	27	2
	6	39-68				
	9	40-69				
DS07	2	56-85	90	63	27	3
	6	45-74				
	9	67-96				

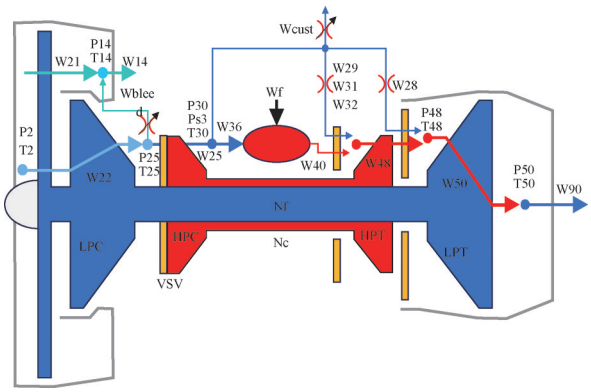

Fig.10 Structural diagram of turbofan engine

3.2.1 Correlation Analysis

There are 32 sensors related to the gas path components in the N-CMAPSS dataset. Nevertheless, owing to the extremely intricate internal structure of the aero-engine, as component coupling intensifies, sensors become more tightly interdependent, greatly enhancing the correlation among their data. In order to efficiently diagnose faults from the sensor data, it is necessary to perform Pearson correlation analysis between the sensors[29]. Figure 11 is a correlation heat map of 32 sensors. It can be seen from the figure that the correlation between the sensors is very high, and the correlation between some sensors even reaches 1.

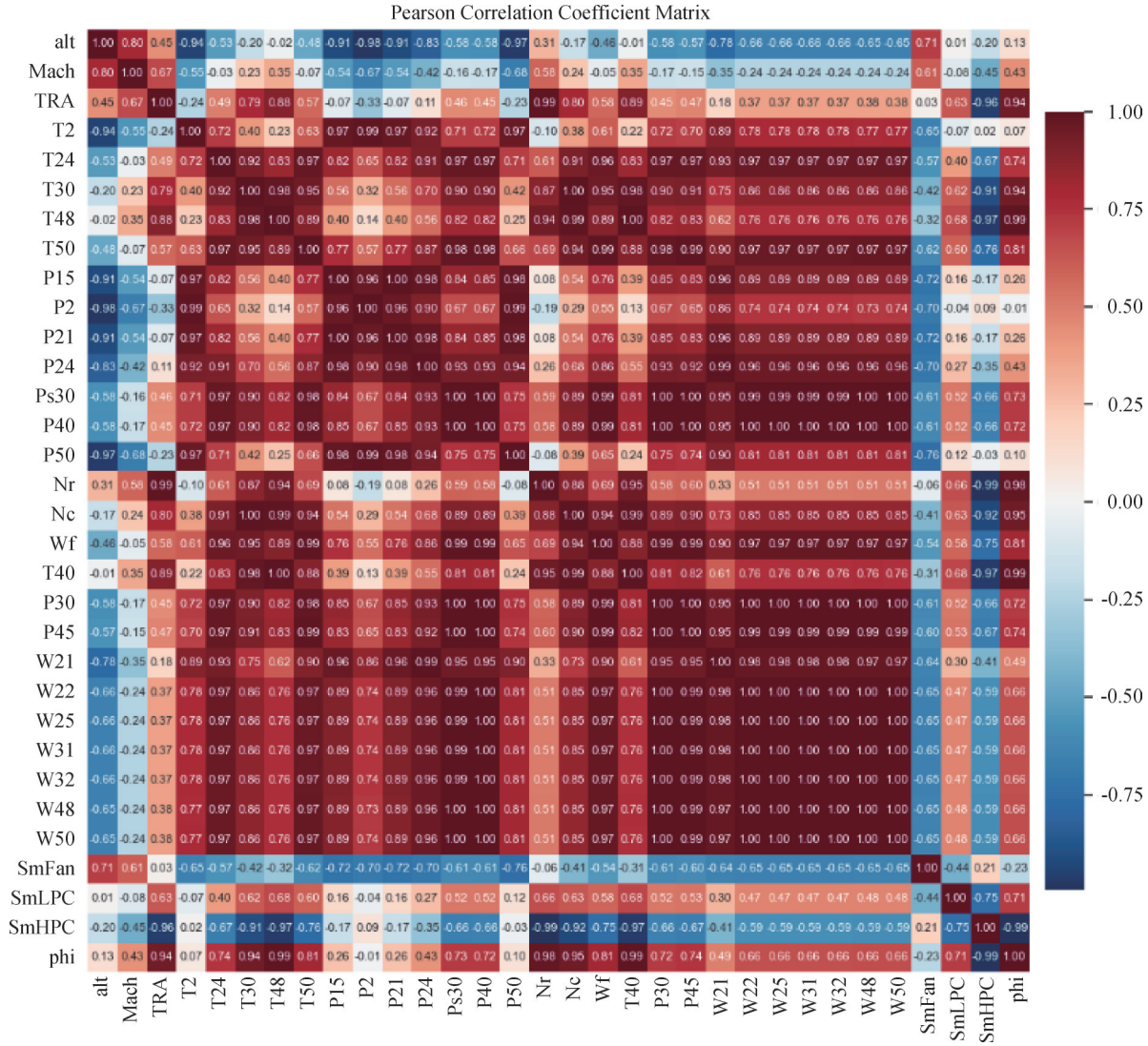

Fig.11 32-channel sensor correlation heat map

To ensure the efficiency of subsequent model operation and the effectiveness of feature extraction, this study removes sensors with values higher than 0.9 from the 32 sensors, leaving 6 sensors as inputs for the subsequent model: flight altitude (Alt), flight Mach number (Mach), throttle solver angle (TRA), low-pressure compressor outlet total temperature (T24), fan stall margin (SmFan), and low-pressure compressor stall margin (SmLPC).

3.2.2 Data Downsampling

The amount of data in aero-engine operation is huge. Traditional data feature extraction will cause data redundancy and high computational cost. In order to quickly extract data features within the aero-engine operation cycle, this study introduces the K-means clustering method[30]. The original dataset, consisting of tens of thousands of samples, was compressed to a standardized 1, 000 samples using the k-means method, significantly reducing the model's computational load. The downsampled standard samples were then fed into the network.This method divides the data into K clusters, compresses the feature space by minimizing the distance within the cluster, uses the cluster center point to represent the local data distribution, maps high-dimensional data to low-dimensional cluster label space, and reduces the amount of data while retaining data features.

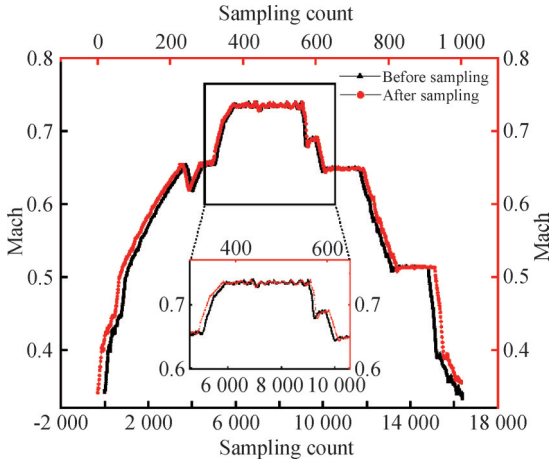

Fig.12 Data downsampling

3.3 Evaluation Indicators

In order to comprehensively evaluate the experimental results of aero-engine gas path fault diagnosis, this study uses accuracy, precision, recall rate and F1 score as evaluation indicators for fault diagnosis[31]. The definition of each evaluation indicator is as follows:

$$\begin{cases} \text{Accuracy} = \dfrac{TP+TN}{TP+FP+TN+FN} \\ \text{Precision} = \dfrac{TP+TN}{TP+FP} \\ \text{Recall} = \dfrac{TP}{TP+TN} \\ \text{F1score} = 2\times\dfrac{\text{Precision}\times\text{Recall}}{\text{Precision}+\text{Recall}} \end{cases} \tag{3}$$

In equation (3), the true positive (TP) indicates the number of correctly classified faulty samples, the true negative (TN) indicates the number of correctly classified non-faulty samples, the false positive (FP) indicates the number of faulty samples incorrectly predicted as fault-free, and the false negative (FN) indicates the number of non-faulty samples incorrectly predicted as faulty.

Accuracy refers to the fraction of correct predictions made by the model, precision indicates the proportion of samples predicted as faulty that are actually faulty, recall quantifies the model's ability to detect positive instances, and the F1 score is the harmonic average of precision and recall, providing a measure of the model's overall performance. In summary, the four evaluation criteria mentioned above can deliver a comprehensive evaluation of the aero-engine fault diagnosis model's performance.

4 Aircraft engine air path fault diagnosis based on FGO-1DCNN-LSTM

To test the efficacy of the FGO-1DCNN-LSTM model for fault diagnosis in aero-engine gas paths, diagnostic analysis was performed on four types of fault data under three different operating conditions. GRU, TCN, 1DCNN, LSTM, and 1DCNN-LSTM were selected as comparative models. First, the GRU and TCN models, which are commonly used in fault diagnosis, were selected as control models to analyze the significance of using convolutional neural networks. Second, 1DCNN, LSTM, and 1DCNN-LSTM models were selected to illustrate the significance of the network combination and parameter optimization used in this study. The parameters in these three models are the same as the corresponding structural parameters in FGO-1DCNN-LSTM to ensure the rigor of the experiment.

4.1 Model Training Under Three Working Conditions

Figure 13 shows the model training accuracy curve and loss function curve under condition A.

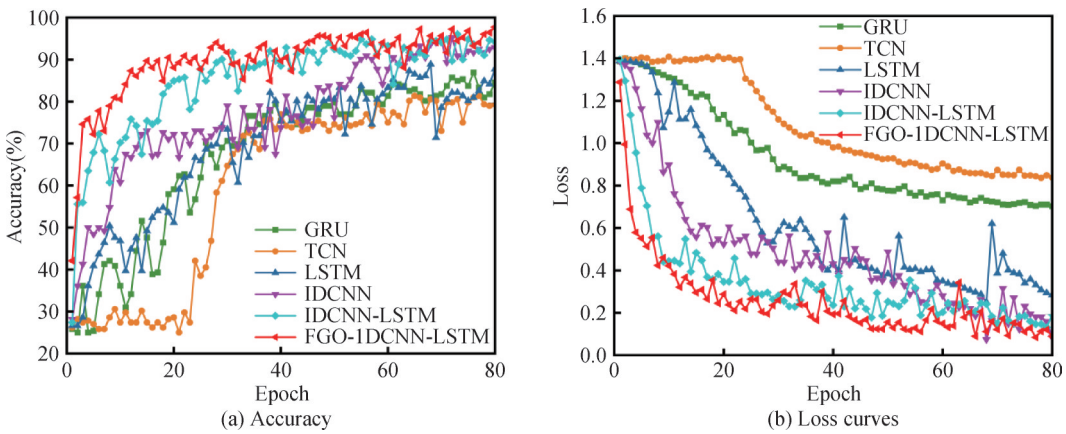

(a) Accuracy (b) Loss curves

Fig.13 Training curve of working Condition A model

Figure 13(a) illustrates the accuracy curves of six models—GRU, TCN, 1DCNN, LSTM, 1DCNN-LSTM, and FGO-1DCNN-LSTM—under condition A. After 80 iterations, the accuracy of all six models stabilized, remaining above 75%. In comparison, the diagnostic performance of GRU, TCN, and LSTM was poor, below 90%. The 1DCNN network with the introduction of a split-path convolution module achieved an accuracy of

92.85%, but its accuracy fluctuated significantly during training. The 1DCNN-LSTM network, which fused LSTM and 1DCNN, further improved the accuracy to 94.84%. Thanks to the parameter optimization of the FGO algorithm, the FGO-1DCNN-LSTM model was the most stable and had the highest accuracy of 97.22% throughout the training process, a 2.38 percentage points increase over the unoptimized model.

Figure 13(b) shows the loss function curves of six models—GRU, TCN, 1DCNN, LSTM, 1DCNN-LSTM, and FGO-1DCNN-LSTM—under condition A. The figure shows that GRU and TCN have the worst convergence performance, while the FGO-1DCNN-LSTM model converges the fastest and stabilizes earliest.

Figure 14 illustrates the model training accuracy curve and loss function curve under condition B.

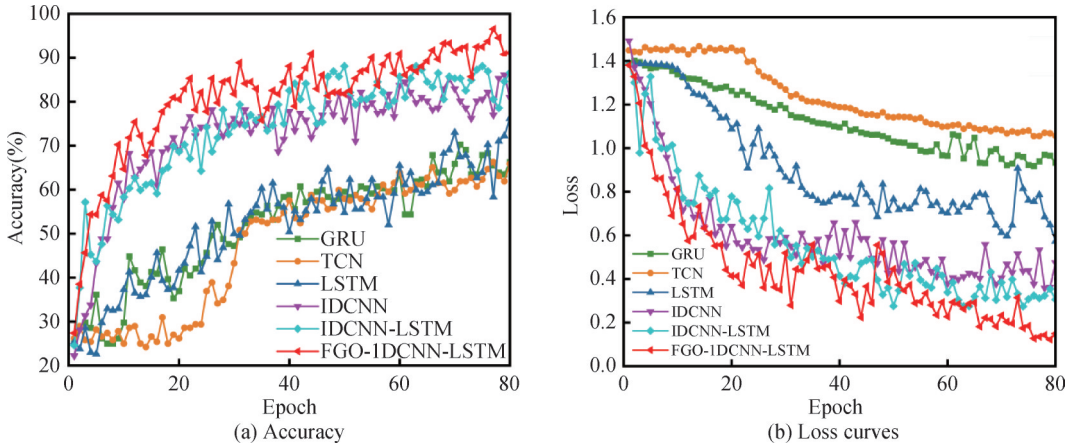

(a) Accuracy (b) Loss curves

Fig.14 Training curve of working Condition B model

Figure 14(a) illustrates the accuracy curves of six models—GRU, TCN, LSTM, 1DCNN, 1DCNN-LSTM, and FGO-1DCNN-LSTM—under scenario B. After 80 iterations, the accuracy curves of all six models tended to stabilize. Among them, the accuracy of GRU, TCN, and LSTM was lower than that of the other three models, with the final result hovering around 70%. 1DCNN-LSTM had slightly higher accuracy than 1DCNN, with the accuracy of the two models being 86.61% and 80.95%, respectively. The FGO-1DCNN-LSTM model, after hyperparameter optimization using the FGO algorithm, achieved a final accuracy of 91.11%, which was 4.50 percentage points higher than the unoptimized accuracy, and it consistently maintained the highest accuracy throughout the entire training process.

Figure 14(b) shows the loss function curves of six models: GRU, TCN, LSTM, 1DCNN, 1DCNN-LSTM, and FGO-1DCNN-LSTM. After 80 iterations, the convergence ability of GRU, TCN, and LSTM models is comparatively low, with loss function values all higher than 0.6. The FGO-1DCNN-LSTM model has the best convergence performance compared to the other models.

Figure 15 illustrates the model training accuracy curve and loss function curve under operating condition C.

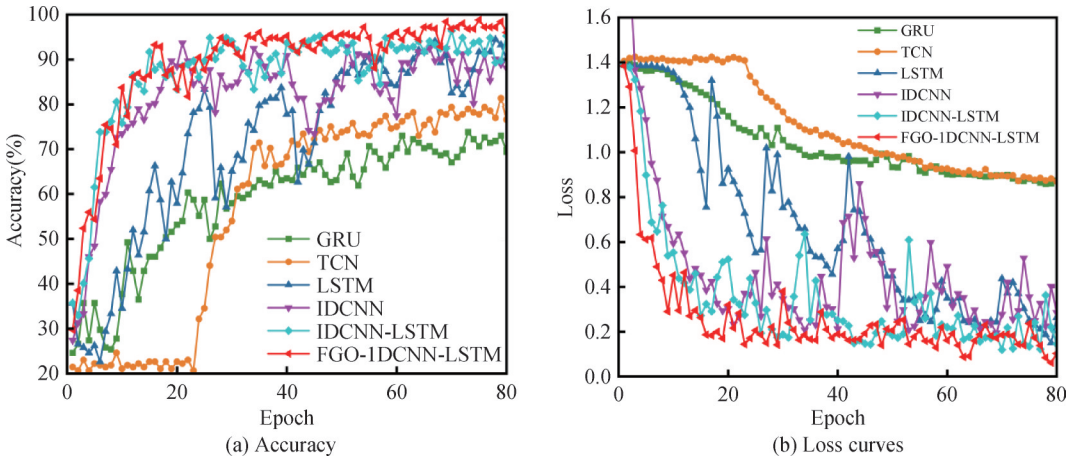

(a) Accuracy (b) Loss curves

Fig.15 Training curve of working Condition C model

Figure 15(a) illustrates the accuracy curves of six models—GRU, TCN, LSTM, 1DCNN, 1DCNN-LSTM, and FGO-1DCNN-LSTM—under scenario C. After 80 iterations, the accuracy of all six models exceeded 75%. In particular, GRU and TCN yielded the poorest performance, with accuracy falling below 80%; LSTM

showed marginally better results, achieving an accuracy of 88.09%, but the curve fluctuated and was not very stable; 1DCNN achieved an accuracy of 90.07%, outperforming LSTM; the fused 1DCNN-LSTM model further improved its overall accuracy to 95.61%; and the FGO-1DCNN-LSTM model, after hyperparameter optimization, achieved an accuracy of 98.41%, and was the first to stabilize during the entire training process, showing a 2.80 percentage points improvement in accuracy compared to the unoptimized model.

Figure 15(b) illustrates the loss rate curves of six models—GRU, TCN, LSTM, 1DCNN, 1DCNN-LSTM, and FGO-1DCNN-LSTM—under condition C. After 80 iterations, the GRU and TCN models converged more slowly, with loss function values all above 0.8, while the loss function values of the other four models were all below 0.3. The FGO-1DCNN-LSTM model had the lowest loss function value, at only 0.1, and converged earliest.

In light of the accuracy and convergence rate of the models above, it is clear that the GRU and TCN models perform poorly. Therefore, these two models will not be analyzed in the model metrics and confusion matrix sections of the diagnostic experiments for the following three operating conditions.

4.2 Four Types of Fault Diagnosis Under Operating Condition A

The trained model was applied to identify faults in the test set under operating condition A. The diagnosis results of the four faults were plotted into a confusion matrix, which can more intuitively show the diagnostic effects of different models, as shown in Figure 16.

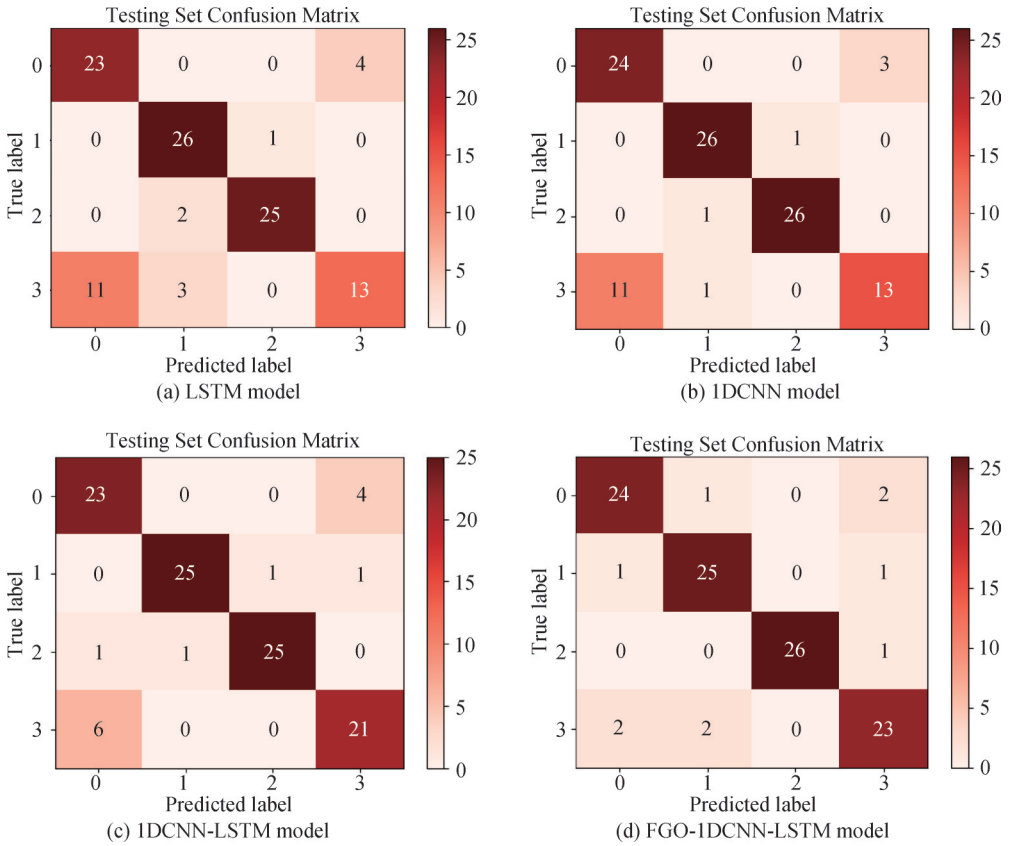

Fig.16 Confusion matrices for working condition A

Figure 16 shows the test set confusion matrices for four models: LSTM, 1DCNN, 1DCNN-LSTM, and FGO-1DCNN-LSTM. All four models are relatively sensitive to faults 1 and 2. The LSTM model is insensitive to faults 0 and 3, with an accuracy of only 79.63%. The 1DCNN model shows an overall improvement in accuracy to 83.33%, but performs poorly with fault 3. The 1DCNN-LSTM combination model further improves accuracy to 87.96%. The FGO-1DCNN-LSTM model has the highest accuracy and best performance, reaching 90.74%, which is 11.11%, 7.41%, and 2.78% higher than the LSTM, 1DCNN, and 1DCNN-LSTM models, respectively.

Figure 17 depicts the evaluation metrics of the four models. The FGO-1DCNN-LSTM model attains the best performance in all four metrics, with Accuracy, Precision, Recall, and F1 score of 90.74%, 90.87%, 90.84%, and 90.81%, respectively.

4.3 Four Types of Fault Diagnosis Under Operating Condition B

The trained model is used to diagnose the test set under working condition B, and the diagnosis results are plotted as a confusion matrix, as shown in Figure 18.

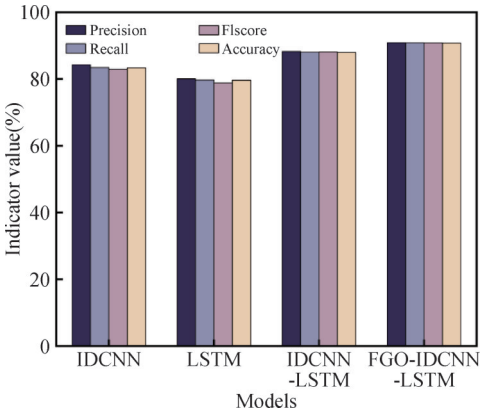

Fig.17 Evaluation Indicators for Working Condition A Model

Figure 18 shows the test set confusion matrices for four models: LSTM, 1DCNN, 1DCNN-LSTM, and FGO-1DCNN-LSTM. All four models generally demonstrate good diagnostic performance for fault 3. The LSTM model is insensitive to both faults 1 and 3, with an accuracy of only 70.37%. The overall accuracy of the 1DCNN model has increased to 73.15%, and the accuracy of the combined 1DCNN-LSTM model is further improved to 81.48%. The FGO-1DCNN-LSTM model performs best, achieving an accuracy of 90.74%, which is 20.37%, 17.59%, and 9.26% higher than the LSTM, 1DCNN, and 1DCNN-LSTM models, respectively.

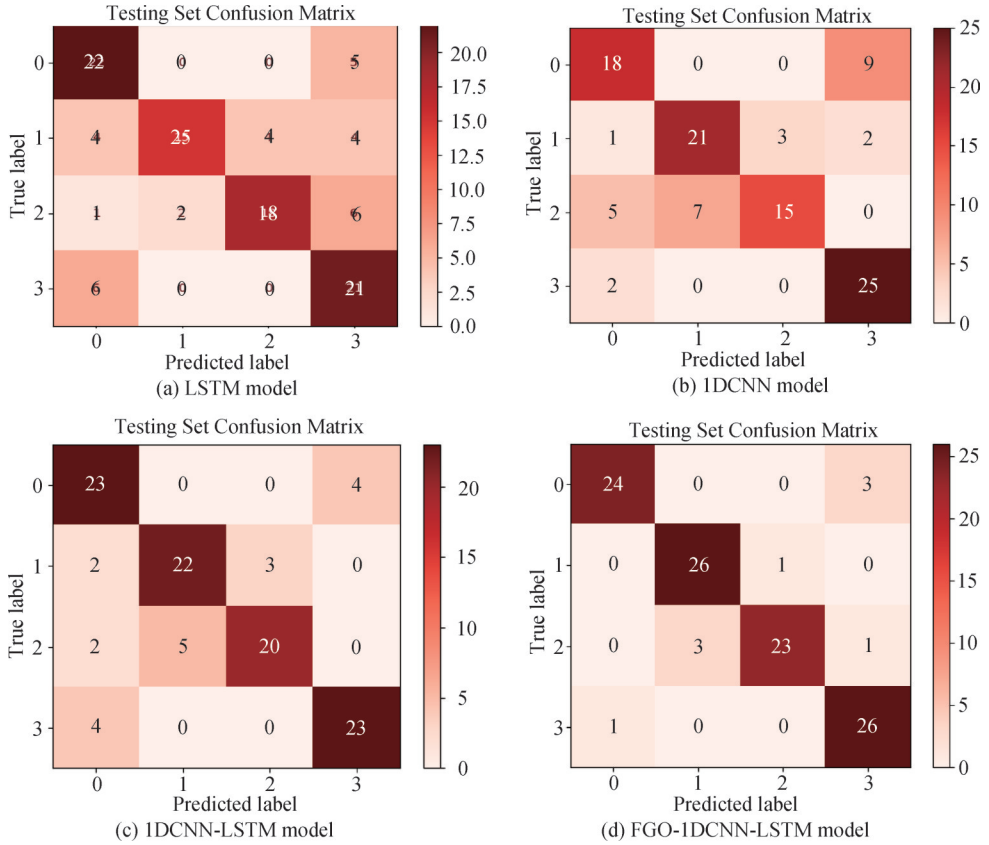

Fig.18 Confusion matrices for working condition B

Figure 19 illustrates the evaluation metrics of the four models. In the evaluation scores, the FGO-1DCNN-LSTM model surpasses the other three models in all evaluation metrics, with Accuracy, Precision, Recall and F1 score of 91.67%, 92.04%, 91.69% and 91.66%, respectively.

4.4 Four Types of Fault Diagnosis Under Operating Condition C

The trained model is used to diagnose the test set under working condition C, and the diagnosis results are plotted as a confusion matrix, as shown in Figure 20.

Figure 20 shows the test confusion matrices of LSTM, 1DCNN, 1DCNN-LSTM, and FGO-1DCNN-LSTM models under different faults. All four models

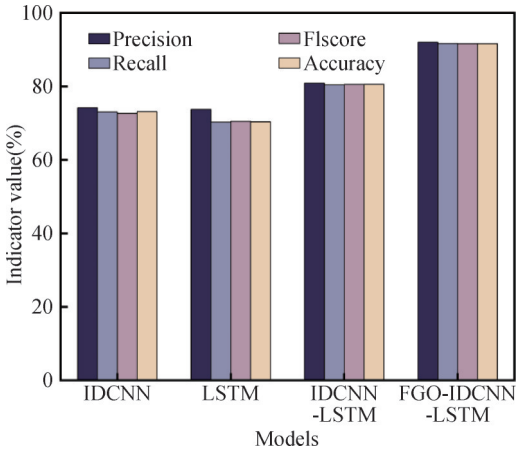

Fig.19 Evaluation indicators of Working Condition B model

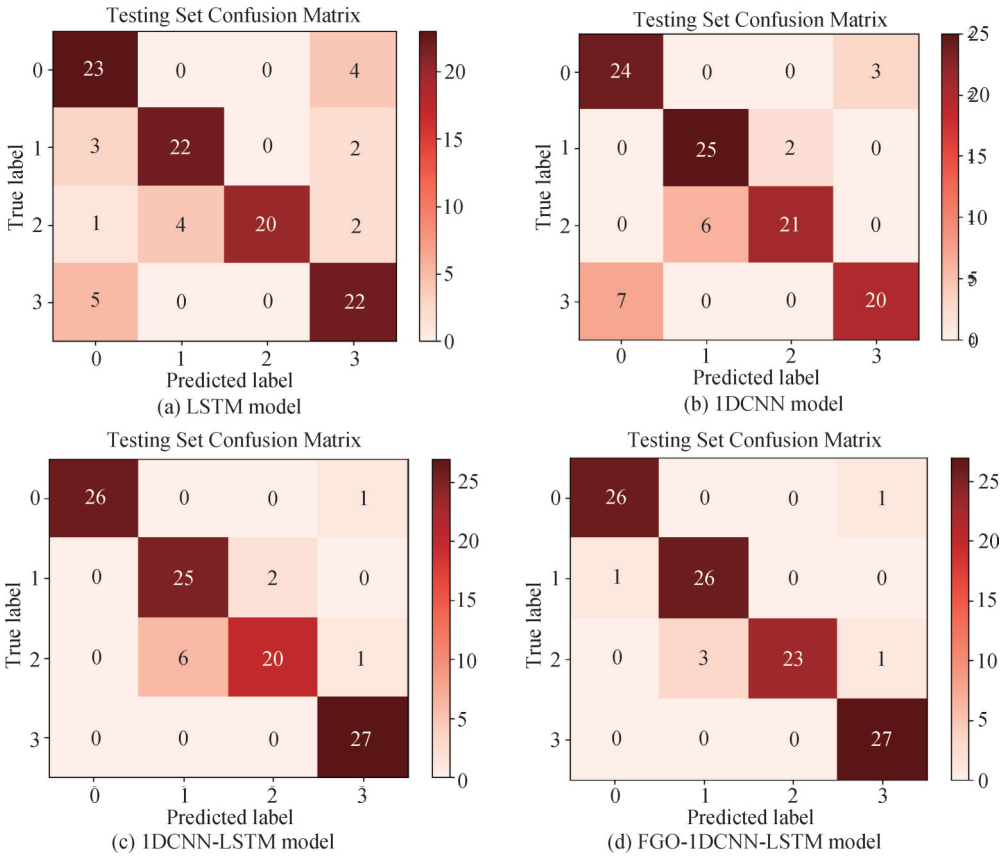

Fig.20 Confusion matrices for working condition C

showed the most stable performance for faults 0 and 1. The LSTM model was insensitive to fault 2, with an accuracy of 80.56%. The 1DCNN model had an overall accuracy of 83.33%, but its diagnostic performance for faults 2 and 3 was poor. The accuracy of the combined 1DCNN-LSTM model was 90.74%. The highest accuracy was achieved by the FGO-1DCNN-LSTM model at 94.44%, which was 13.88%, 11.11%, and 3.7% higher than the LSTM, 1DCNN, and 1DCNN-LSTM models, respectively, but its diagnostic performance for fault 2 was unsatisfactory.

The evaluation metrics for the four models are shown in Figure 21. The FGO-1DCNN-LSTM model has the highest evaluation metrics, with Accuracy, Precision, Recall and F1 score of 94.44%, 94.54%, 94.34% and 94.32%, respectively.

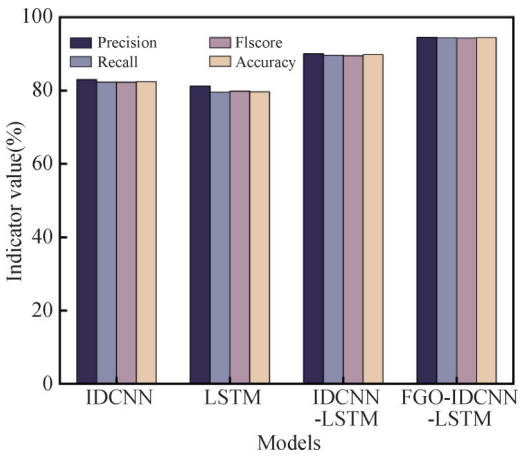

Fig.21 Evaluation indicators of Working Condition C model

5 Conclusion

This study proposes an FGO-1DCNN-LSTM fault diagnosis model for diagnosing aero-engine gas path faults. This model leverages the ability of LSTM to handle long-term dependencies between time-series data, compensating for the limitations of 1DCNN in feature extraction over the temporal dimension. Furthermore, a feature fusion module is introduced into the 1DCNN model to further enhance the network's feature extraction capabilities. The FGO algorithm is incorporated into the 1DCNN-LSTM model to construct the FGO-1DCNN-LSTM model, thereby addressing the issue of hyperparameter optimization in deep learning models. Results show that the trained FGO-1DCNN-LSTM model exhibits excellent performance, achieving accuracy rates of 90.74%, 91.67%, and 94.44%, respectively. In comparison with the 1DCNN-LSTM model without the FGO algorithm, the proposed model achieves accuracy improvements of 2.78%, 10.19%, and 3.7%, respectively. The FGO-1DCNN-LSTM model demonstrates enhanced stability, convergence, and stronger generalization abilities. Comparison of experimental results across three operating conditions reveals that the model's diagnostic accuracy gradually increases with the improvement of the

aero-engine's operating condition level. This is because the characteristics of fault signals become easier to identify with higher operating condition levels. This study can act as an important addition to current aero-engine condition monitoring and fault diagnosis systems, offering guidance for the optimal performance of aero-engines.

Author Contribution:

Luyao He: Supervision, Resources, Project administration, Funding acquisition. Mingzheng Liu: Writing – review & editing, Writing –original draft, Data analysis. Ximeng Wang: Investigation and analysis. Bo Hu: Data organization. Bin Liu: Validation, Funding acquisition. Siying Guo: Supervision, Resources, Project administration.

Foundation Information:

This work was supported by the National Natural Science Foundation of China under Grant nos. 62301341, 62371315 and 62531017, by the Liaoning Provincial Department of Science and Technology (Applied Basic Research) under Grant nos. 2025JH2/101300013, and by the Youth Project of Liaoning Provincial Department of Education under Grant nos. 200080762/070.

Data Availability:

The authors declare that the main data supporting the findings of this study are available within the paper and its Supplementary Information files.

Conflicts of Interest:

The authors declare no competing interests.

Dates:

Received April 2, 2026; Accepted May 21, 2026; Published online July 10, 2026.

References

[1] Weitong Liu, Guoqlang Xu, Xiuting Gu, et al. Experimental analysis and thermodynamic modeling for multilevel heat exchange system with multifluid in aero engines[J]. *Energy* , **2025**,315(Jan..15):134373.1-134373.19

[2] Haoming Miao; Chao Li; Linjian Lao; Jie Hong;Yanhong Ma. Research on the failure mechanism in the convergent section of an aero-engine's adjustable nozzle under multi-field coupling analyses[J]. *Engineering Failure Analysis*. **2025**: 109176.

[3] Guan, Hong; Ni, Kaixuan; Ma, Hui; Xiong, Qian; Wang, Weiwei; Wang, Hongji. Dynamic modeling and verification of rotating compressor blade with crack based on beam element[J]. *Applied Mathematical Modelling. Simulation and Computation for Engineering and Environmental Systems*. **2024**: 367-393.

[4] Bingyin Lei; Ning Shen; Dengyi Ji; Ruizhi Ouyang; Li Yang; Qiming Liu; Bingrui Gao; Ziyang Wang. A Comprehensive Review of Key Technologies for Enhancing the Reliability of Aero-Engines[J].*IEEE Access*. **2024**:148315-148331.

[5] Chenyu Gan, Shuiting Ding, Tian Qiu, et al. Model-based safety analysis with time resolution (MBSA-TR) method for complex aerothermal-mechanical systems of aero-engines[J]. *Reliability engineering & system safety*, **2024**, 243(Mar.): 109864.1-109864.18.

[6] Jian Chen, Kening Yuan, Linbo Zhu, et al. Dynamic modelling and stability analysis of aero-engine rotor system considering aerodynamics[J]. *Aerospace science and technology*, **2024**, 151 (Aug.): 109294.1-109294.18.

[7] ALLAN J. VOLPONI. Gas Turbine Engine Health Management: Past, Present, and Future Trends[J]. *Journal of engineering for gas turbines and power: Transactions of the ASME*,**2014**, 136 (5): 051201-1-051201-20.

[8] Kong, Changduk. Review on Advanced Health Monitoring Methods for Aero Gas Turbines using Model Based Methods and Artificial Intelligent Methods [J]. *International Journal of Aeronautical and Space Sciences*. **2014**, Vol. 15(No. 2): 123-137.

[9] Bai, Mingliang, Liu,et al. Anomaly detection of gas turbines based on normal pattern extraction[J]. *Applied thermal engineering:Design*, processes, equipment, economics, **2020**,166.

[10] Long Chen, Yuchuan Zhu, Jie Ling, et al. Temperature dependence modeling and experimental evaluation of a multidimensional discrete magnetostrictive actuator[J]. *Applied thermal engineering: Design* , processes, equipment, economics, **2023**, 230(Pt.B): 120736-1-120736-12.

[11] Anthony Siming Chen; Guido Herrmann; Reza Islam; Matthew Turner; Chris Brace; Giovanni Vorraro; James W.G. Turner; Stuart Burgess; Nathan Bailey. Effective emission control of aero-engines via nonlinear dual-estimators for uncertain states and parameters[J]. *Aerospace Science and Technology* .**2025**:110210.

[12] Jia Z H, Shao D, Dong P C, et al. Development of Performance Analysis Technology for Engine Modification Applied to High-Altitude UAVs[J]. *Aerospace Power*, **2024**, (06): 28-31.

[13] Rath, Naraharia, bCAa; Mishra R. K. *cCAb*; Kushari, AbhijitbCAc. Aero engine health monitoring, diagnostics and prognostics for condition-based maintenance: an overview[J]. International Journal of Turbo and Jet Engines. **2023**, Vol. 40 (No.1):S279-S292.

[14] Huang Jinquan, Wang Qihang, Lu Feng. Research Status and Prospect of Aero-Engine Gas Path Fault Diagnosis[J]. *Journal of Nanjing University of Aeronautics and Astronautics*, **2020**, 52(04): 507-522.

[15] Xiaoyu Wang1. Aero Engine Fault Diagnosis Based on Support Vector Machine[J]. *Procedia Computer Science* , 2025,Vol.262: 1352-1358

[16] Jinghui Xu; Ye Wang; Zepeng Wang; Xizhen Wang; Yongjun Zhao. Transient gas path fault diagnosis of aero-engine based on domain adaptive offline reinforcement learning[J].

Aerospace Science and Technology. **2024**, Vol. 155(Part 3): 109701.

[17] Yu-Qiang Wang; Bo-Yu liang; Yu-Wei Wang; Chen-Yang Zhang; Yong-Ping Zhao. A novel data-driven method for aero-engine performance degradation trend prediction under various operating conditions[J]. *Mechanical Systems and Signal Processing*. **2025**:112856.

[18] Yusra Abdulrahman; M. A Mohammed Eltoum; Abdulla Ayyad; Brain Moyo; Yahya Zweiri. Aero-engine Blade Defect Detection: A Systematic Review of Deep Learning Models [J]. *IEEE Access*. **2023**:1.

[19] Yin G, Zhu M, Yan Y H, et al. DMIFD: A Deep Learning-Based Multimodal Industrial Fault Diagnosis Method[J]. *Chinese Journal of Scientific Instrument*, **2025**, 46(06): 215-227.

[20] Jiao W D, Lin S S. An Overall Improved Fault Diagnosis Method Based on Support Vector Machine[J]. *Chinese Journal of Scientific Instrument*, **2015**, 36(08): 1861-1870.

[21] Mohaimenul Azam Khan Raiaan; Sadman Sakib; Nur Mohammad Fahad; Abdullah Al Mamun; Md. Anisur Rahman; Swakkhar Shatabda; Md. Saddam Hossain Mukta. A systematic review of hyperparameter optimization techniques in Convolutional Neural Networks[J]. *Decision Analytics Journal*. **2024**:100470.

[22] Yao G, Lei T, Zhong J. A review of convolutional-neural-network-based action recognition. *Pattern Recogn Lett* **2019**; 118:14-22.

[23] Yu X X, Tang B P, Wei J, et al. Fault Diagnosis Method for Aero-Engine Accessory Gearbox Based on Adaptive Graph Convolutional Neural Network Under Strong Background Noise[J]. *Chinese Journal of Scientific Instrument*, **2021**, 41 (08): 78-86.

[24] Yu Y, Si X, Hu C, et al. A review of recurrent neural networks: LSTM cells and network architectures. *Neural Comput* **2019**; 31(7):1235–70.

[25] Yin G, Zhu M, Quan P C, et al. Research on Electrolysis Temperature Prediction Method of Aluminum Electrolytic Cell Based on PID Search Optimization for CNN-LSTM-Attention[J]. *Chinese Journal of Scientific Instrument*, **2025**, 46(01): 324-337.

[26] Sulaiman M H, Mustaffa Z, Mohamed M R, et al. Fungal growth optimizer: A novel nature-inspired metaheuristic algorithm for solving optimization problems[J]. *IEEE Access*, **2020**, 8: 144 698-144 718.

[27] Fang Dao, Yun Zeng, Jing Qian. Fault diagnosis of hydro-turbine via the incorporation of Bayesian algorithm optimized CNN-LSTM neural network[J]. *Energy*, **2024**, 290(Mar. 1): 130326.1-130326.18.

[28] Qiao H H, Zhao E X, Hao R J, et al. Fault Diagnosis of Bearings Under Variable Operating Conditions Based on Attention Mechanism and Multi-Source Information Fusion [J]. *Chinese Journal of Scientific Instrument*, **2024**, 45(09): 120-130.

[29] Helmy Rahadian; Steven Bandong; Augie Widyotriatmo; Endra Joelianto. Image encoding selection based on Pearson correlation coefficient for time series anomaly detection [J]. *Alexandria Engineering Journal*. **2023**, Vol. 82(Suppl C): 304-322.

[30] Shijie Zhao; Ronghua Yang; Fanshuai Meng; Liang Cai. Optimizing Cluster Centroids with Improved Quadratic Interpolation: An Adaptive K-means Algorithm[J]. *Journal of Computational and Applied Mathematics* .**2025**:116921.

[31] Jonne van Dreven; Abbas Cheddad; Sadi Alawadi; Ahmad Nauman Ghazi; Jad Al Koussa; Dirk Vanhoudt. From data scarcity to diagnostic precision: A novel data augmentation and fault diagnosis framework for district heating substations [J]. *Engineering Applications of Artificial Intelligence*. **2025**: 110662.